Analytic and Experimental Investigation of Beamforming Algorithms for MM-Wave Channel Characterization

Zhang, Fengchun; Fan, Wei; Pedersen, Gert F.

Published in:
2017 11th European Conference on Antennas and Propagation (EUCAP)

DOI (link to publication from Publisher):
10.23919/EuCAP.2017.7928439

Publication date:
2017

Document Version
Early version, also known as pre-print

Analytic and Experimental Investigation of Beamforming Algorithms for MM-Wave Channel Characterization

Fengchun Zhang, Wei Fan, Gert F. Pedersen
Antennas, Propagation and Radio Networking section, Department of Electronic Systems, Aalborg University, Denmark
E-mail: {fz, wfa, gfp}@es.aau.dk

***Abstract*—Beamforming algorithms are expected to be extensively utilized in mm-wave systems to improve system performance. In this paper, we discuss three different beamforming algorithms based on uniform circular arrays (UCAs), i.e. classicial beamfomer, coventional frequency invariant beamformer. Numerical simulation results and channel sounding measurement results at mm-wave are provided to demonstrate and compare the performance of the different beamformers in channel parameter estimation applications.**

***Index Terms*—beamforming, uniform circular arrays, mm-wave.**

I. Introduction

To meet the continuously increasing demands for high data rate in mobile communications, the exploitation of the huge unlicensed frequency bands has attracted more and more interests [1]. Accurate channel characterization is important for future 5G systems design and performance analysis [2]. So far, high gain directional antennas have been extensively used in channel measurements at mm-wave frequency bands, mainly due the link budget issue, high cost of massive antenna arrays at mm-wave bands and lack of wideband channel estimation algorithms for massive arrays [3], [4]. However, such mechanical steering measurement systems suffer from considerable measurement time, limited spatial resolution and etc. The small wavelength of 5G systems increases the possibility of implementation massive antenna arrays both at the mobile devices and base station, which makes beamforming technique an attractive solution. With antenna array, beams can be electronically steered via controlling antenna element weights. Further, pencil beam pattern becomes a reality with a sufficient number of antenna elements at mm-Wave bands.

Different from linear arrays and rectangular arrays, the uniform circular arrays (UCAs) can achieve approximately uniform beam patterns around the UCA plane. Furthermore, by applying the frequency invariant beamformers (FIBFs) based on UCAs, the beam patterns are invariant over wide frequency bands, which can be used for broadband channel estimation [6], [7], [9], [11]. However, most of the UCA FIBF investigations are based on the 2D assumption (i.e. all paths are strictly on the UCA plane) and only demonstrated by simulation results [6], [7], [11]. In [10], a modified FIBF (MFIBF) which is suitable for 3D propagation channels, was proposed and validated by channel sounding measurements.

To our knowledge, a comprehensive analysis of the UCA with classical beamformer (CBF), conventional FIBF (CFIBF) and MFIBF for both 2D and 3D scenarios is missing. In this paper, we first summarize the CBF, CFIBF and MFIBF for UCAs in both 2D and 3D scenarios. After that, the performance of these BFs are demonstrated and compared by simulation results and channel sounding measurement results.

II. Problem Statement

Assume that a UCA, composed of P isotropic antenna elements uniformly distributing along the circle of radius r, is lying on the xy plane. The center of the UCA is located at the origin of the coordinate systems. K paths impinging upon the UCA are assumed, where the incident angle of the k-th path is (θ_k, ϕ_k). The elevation angle $\theta \in [0, \pi/2]$ is measured downward from the z-axis, and the azimuth angle $\phi \in [0, 2\pi]$ is measured counter-clockwise from the x-axis on the xy plane. The frequency response at the UCA center can be expressed as,

$$\mathbf{H}(f) = [\alpha_1 \exp(-j2\pi f\tau_1), ..., \alpha_K \exp(-j2\pi f\tau_K)]^T, \quad (1)$$

where α_k and τ_k represent the complex amplitude and delay of the k-th path ($k \in [1, K]$), respectively. $f \in [f_L, f_U]$ is the frequency of interest. $(\cdot)^T$ denotes the transpose operator. The frequency response of the UCA elements can be given by

$$\mathbf{H}_{el}(f) = \mathbf{A} \cdot \mathbf{H}(f), \quad (2)$$

where $\mathbf{A}$ is the array manifold matrix defined as

$$\mathbf{A} = [\mathbf{a}(f, \theta_1, \phi_1), ..., \mathbf{a}(f, \theta_K, \phi_K)], \quad (3)$$

with $\mathbf{a}$ expressed as

$$\begin{aligned}\mathbf{a}(f, \theta, \phi) =& [\exp(\frac{j2\pi fr}{c} \sin\theta \cos(\phi - \varphi_1)), \\ & ..., \exp(\frac{j2\pi fr}{c} \sin\theta \cos(\phi - \varphi_P))],\end{aligned} \quad (4)$$

where $\varphi_p = 2\pi \cdot (p-1)/P$, $p \in [1, P]$ is the angular position of the p-th element.

To align the phases of elements and synthesis the beam pattern of the UCA, a complex weight vector $\mathbf{W}(f,\theta,\phi)$ is introduced. We can obtain the beam pattern of the UCA as,

$$\begin{aligned} H_F(f,\theta,\phi) &= \mathbf{W}(f,\theta,\phi)\cdot\mathbf{H}_{el}(f) \\ &= [\mathbf{W}(f,\theta,\phi)\cdot\mathbf{A}]\cdot\mathbf{H}(f) \\ &= \mathbf{V}(f,\theta,\phi)\cdot\mathbf{H}(f), \end{aligned} \tag{5}$$

where the term of $[\cdot]$ is replacing by vector $\mathbf{V}(f,\theta,\phi)$. $v^k(f,\theta,\phi)$ represents the k-th element of vector $\mathbf{V}(f,\theta,\phi)$. The corresponding channel impulse response (CIR) can be calculated by taking the IDFT of $H_F(f,\theta,\phi)$, as

$$h(t,\theta,\phi) = \sum_{f=f_L}^{f_H} H_F(f,\theta,\phi)\exp(j2\pi ft). \tag{6}$$

The main target is to detect the path parameters $\{\alpha_k,\tau_k,\phi_k\}$ with arbitrary θ_k presents. The detection accuracy of the k-th path relies on:

- A peak $v^k(f,\theta,\phi)=1$ exists at $\phi=\phi_k$;
- The interfering beam patterns $v^k(f,\theta,\phi),\phi\neq\phi_k$ and $v^i(f,\theta,\phi_k), i\neq k$ approach 0.

A. Classical Beamformer (CBF)

For CBF methods with uniform amplitude weighting, we choose the weight vector in (5) as

$$\mathbf{W}(f,\theta,\phi) = \frac{1}{P}\mathbf{a}^H(f,\theta,\phi), \tag{7}$$

where $(\cdot)^H$ denotes the Hermitian transpose operator. According to [8], $v^k(f,\theta,\phi)$ in (5) can be rewritten as

$$\begin{aligned} &v^k_{CB}(f,\theta,\phi) \\ &= J_0\Big(\frac{2\pi fr\sqrt{\sin^2\theta - 2\sin\theta\sin\theta_k\cos(\phi-\phi_k)+\sin^2\theta_k}}{c}\Big). \end{aligned} \tag{8}$$

$J_n(\cdot)$ is the Bessel function of the first kind with order n.

1) CBF for 2D scenario: If all of the paths are restricted on the UCA plane (i.e. $\theta_k = 90^o, k\in[1,K]$), we have $\mathbf{W}(f,\theta,\phi)=\mathbf{W}(f,\frac{\pi}{2},\phi)$. Then (8) can be simplified as,

$$v^k_{CB,2D}(f,\phi) = J_0\Big(\frac{2\pi fr}{c}\mid\sin\Big(\frac{\phi-\phi_k}{2}\Big)\mid\Big). \tag{9}$$

As demostrated in Section III and IV, the beam patterns of CBF are frequency dependent and the sidelobes are high [11].

2) CBF for 3D scenario: For a more general case, we have at least one path out of the UCA plane (i.e. $\theta_k\neq 90^o, k\in[1,K]$). If $\mathbf{W}(f,\frac{\pi}{2},\phi)$ is also applied, then (8) can be calculated as,

$$\begin{aligned} &v^k_{CB,3D}(f,\frac{\pi}{2},\phi) \\ &= J_0\Big(\frac{2\pi fr\sqrt{1-2\sin\theta_k\cos(\phi-\phi_k)+\sin^2\theta_k}}{c}\Big). \end{aligned} \tag{10}$$

As shown in Fig. 1, the beam patterns of CBF degrade as the θ increases. We can see that the path with $\theta=120^o$ could not be detected. However, the lobes of this path are quite lower. That is, the other paths on the UCA plane can still be detected, since the interfering patterns of the undetectable paths are rather weak.

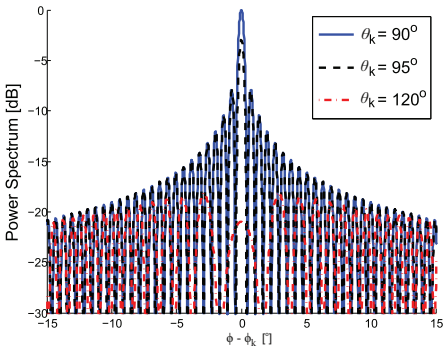

Fig. 1. The beam pattern $v^k_{CB,3D}(f,\phi)$ with $\theta_k=90^o$, 95^o and 120^o.

B. Frequency invariant Beamformer (FIBF)

The beam patterns of FIBFs are approximately frequency independent and constant over the UCA plane. As explained in [9], [11], the element response (2) can be converted to phase mode response and then a proper compesation filter $G_m(f,\theta)$ is chosen to remove the frequency dependency of the beam patterns. Based on [9], [10], the p-th element of vector $\mathbf{W}$ is

$$w^p(f,\theta,\phi) = \sum_{m=-M}^{M}\frac{G_m(f,\theta)}{P(2M+1)}\exp(-jm(\phi-\varphi_p)). \tag{11}$$

We can then obtain the $v^k(f,\theta,\phi)$ of FIBF as,

$$\begin{aligned} v^k_{FI}(f,\theta,\phi) = \sum_{m=-M}^{M}&\frac{\exp(-jm(\phi-\phi_k))}{2M+1} \\ &\cdot j^m J_m(2\pi f(r/c)\sin\theta_k)\cdot G_m(f,\theta). \end{aligned} \tag{12}$$

1) Conventional FIBF for 2D scenario: For 2D scenario, by substituting the compesation filter $G_m(f,\pi/2) = 1/[j^m J_m(2\pi fr/c)]$ in (12), we have

$$v^k_{FI,2D}(f,\phi) = \frac{1}{2M+1}\frac{\sin[(M+\frac{1}{2})(\phi-\phi_k)]}{\sin[\frac{1}{2}(\phi-\phi_k)]}. \tag{13}$$

The frequency-independency of the beam patterns can be explained by equation (13). The FIBF method is superior to CBF in 2D scenarios, as the beam patterns are frequency-invariant and the sidelobes are much lower than that of CBF pattern, which can be demonstrated in Section III.

2) Conventional FIBF for 3D scenario: Similar to the discussion in [10], if $G_m(f,\pi/2)$ is still chosen for 3D scenarios, the beam pattern term (12) can be written as

$$\begin{aligned} v^k_{FI,3D}(f,\phi) = \sum_{m=-M}^{M}&\frac{\exp(-jm(\phi-\phi_k))}{2M+1} \\ &\cdot\frac{j^m J_m(2\pi f(r/c)\sin\theta_k)}{j^m J_m(2\pi f(r/c))}. \end{aligned} \tag{14}$$

The beam patterns of $v^k_{FI,3D}(f,\phi)$ with $\theta_k=90^o, 95^o$ and 120^o are illustrated in Fig. 2 [10]. Similar to the beam patterns

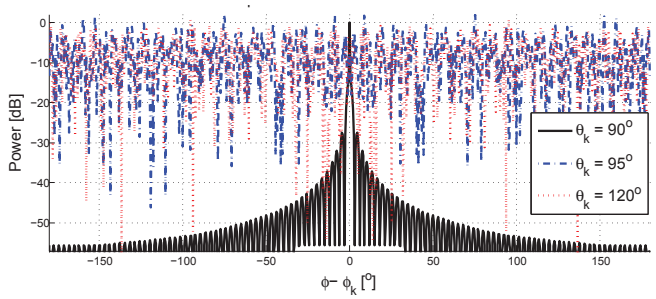

Fig. 2. The beam pattern $v^k_{FI,3D}(f,\phi)$ with $\theta_k = 90^o$, 95^o and 120^o.

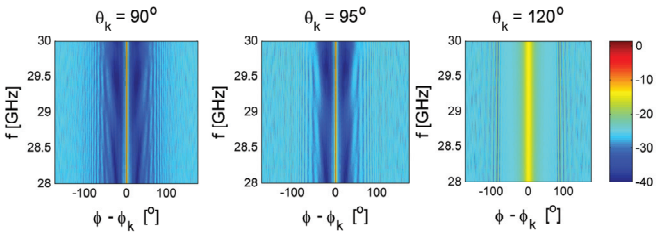

Fig. 3. The beam pattern $\hat{v}^k_{FI,3D}(f,\phi)$ with $\theta_k = 90^o$ (left), 95^o (middle) and 120^o (right) for $f = 28-30$ GHz.

of $v^k_{CB,3D}(f,\phi)$, the beam patterns of $v^k_{FI,3D}(f,\phi)$ deteriorate as θ_k gets larger. We can see that the path with $\theta = 95^o$ could not be detected. Even worse, the lobes of these paths are very high. That is, if there exists a path not strictly in the UCA plane, none of the paths can be detected, since the interferences of these undetectable paths are too high.

As summarized in [10], the conventional FIBF would fail to detect any path if one of the paths is not strictly confined in a same elevation angle, which has limited its applications in practice. The reasons were discussed in detail in [10].

3) Modified FIBF for 3D scenario: To adopt the FIBF methods in practice, a modified FIBF (MFIBF) was proposed in [10]. The proposed compensation filter is given as

$$\hat{G}_m(f) = 1/[0.5j^m(J_m(2\pi fr/c) - jJ_m^{'}(2\pi fr/c)], \quad (15)$$

where $(\cdot)^{'}$ is the differential operator. Comparing with the error introduced by aforementioned $G_m(f,\pi/2)$, the compensation error caused by $\hat{G}_m(f)$ could be reduced to a large extent. Substituting $\hat{G}_m(f)$ for $G_m(f,\pi/2)$ in (14), we have

$$\hat{v}^k_{FI,3D}(f,\phi) = \sum_{m=-M}^{M} \frac{\exp(jm(\phi-\phi_k))}{2M+1}\hat{G}_m(f) \cdot j^m J_m(2\pi f(r/c)\sin(\theta_k)). \quad (16)$$

The beam pattern of $\hat{v}^k_{FI,3D}(f,\phi)$ with $\theta_k = 90^o$, 95^o and 120^o for 28-30GHz are shown in Fig. 3 [10]. Unlike the beam patterns of $v^k_{FI,3D}(f,\phi)$, a peak can be found at $\phi = \phi_k$ with MFIBF. Similar beam patterns of $\hat{v}^k_{FI,3D}(f,\phi)$ can be achieved for $\theta_k = 90^o$, 95^o and 120^o. However, the main beams become wider and more attenuated and the sidelobes around $\phi = \phi_k \pm \pi$ become higher as $|\theta_k - \pi/2|$ increases, due to the remaining error of $|\hat{G}_m(f)\cdot j^m J_m(2\pi fr/c\cdot\sin\theta) - 1|$.

TABLE I
CHANNEL PARAMETERS FOR 2D & 3D SCENARIOS

Path	1	2	3
α / dB	0	-12	-20
τ / ns	10	18	30
$\phi/^o$	180	45	240
$\theta/^o$ for 2D	90	90	90
$\theta/^o$ for 3D	90	95	120

III. Simulation Results

A UCA lying on the xy plane is utilized for simulation and channel sounding measurement. The UCA composes of $p = 720$ isotropic antenna elements, uniformly locating along the circle of radius $r = 0.5$m. The frequency $f \in [28, 30]$GHz with $L = 750$ samples is set.

For 2D scenarios, three paths impinging upon the UCA are assumed, where the parameters of each path are summarized in TABLE I. Fig. 4 shows the power-angle-frequency (PAF) profile and power-angle-delay (PAD) profile with CBF (top), conventional FIBF (middle) and MFIBF (bottom) for 2D scenarios, respectively. As discussed in [11], the beam patterns of the CBF are frequency-dependent and high sidelobes in both frequency (left) and delay (right) domain can be seen. Therefore weak paths may be buried and the estimated amplitudes $\hat{\alpha_k}$ of the weak paths are not accurate due to the high sidelobes of the stronger paths. By applying conventional FIBF, the beam patterns are frequency-invariant, very low sidelobs and almost perfect resolution in both frequency and delay domain can be observed. That is, all of the paths with large dynamic range (e.g. up to $30dB$) can be detected with higher accuracy by applying conventional FIBF. While applying MFIBF, the beam patterns are approximately frequency independent and good resolution in both frequncy and delay domain can be achieved. However, the method suffers from the sidelobes of path 1 (around 0^o and 360^o), as explained in section II.

For 3D scenarios, we assume three paths impinging upon the UCA, where the parameters of each path are summarized in TABLE I. The corresponding results are shown in Fig. 5. We can see that the PAF profile and PAD profile with CBF (top) are very similar for 2D scenarios and 3D scenarios. However, for 3D scenarios, the peak of path 2 decreases and the path 3 disappears due to the elevation angles exists, as explained by Fig. 1. With conventional FIBF (middle), it fails to detect any paths, as expected. With MFIBF (bottom), all of the paths can be detected, though the patterns suffer from the sidelobes around $\phi = \phi_k \pm \pi$.

IV. Measurement Results

For 3D scenarios, the performance of the CBF and MFIBF can be further demonstrated by channel sounding measurement results in a line of sight (LOS) secnario. The description of the measurement campaign is only outlined here, more details can be found in [12]. The transmitter (Tx) was a vertically polarized wideband Biconical antenna. Two sets of measurements were performed by using two types of polarized

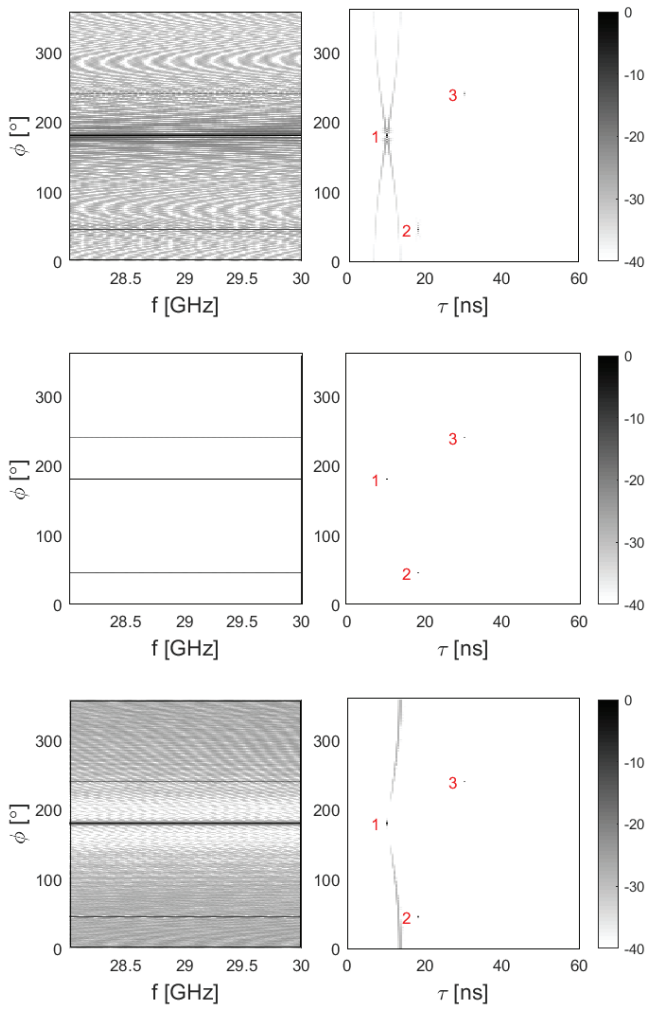

Fig. 4. Performance of CBF (top), conventional FIBF (middle) and MFIBF (bottom) for 2D scenarios.

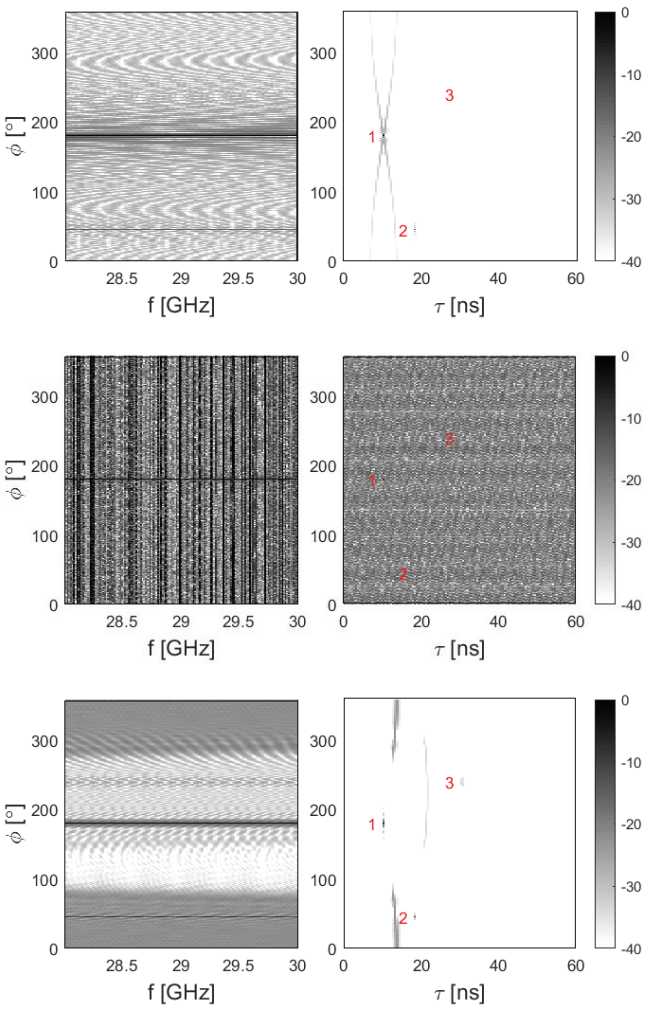

Fig. 5. Performance of CBF (top), conventional FIBF (middle) and MFIBF (bottom) for 3D scenarios.

antennas as the receiver (Rx). In the first measurement, the Rx was a virtual UCA of radius r, which was realized by rotating a Biconical antenna mounted on a positioning turntable. In the second measurement, the Rx was a horn antenna mounted at the center of the turntable. $P = 720$ positions were obtained by automatically repositioning the Rx antenna at uniform angles for both measurements. At each position, the frequency response ($f \in [28, 30]$GHz with 750 samples) at the elements $H_{el}(f)$ were recored. By performing the IDFT of the recored $H_{el}(f)$ at different element positions, the CIRs can be obtained as shown in [12] (Figure 15). One dominant path and a few specular paths can be identified for Biconical CIRs. Note that the dynamic power range limited to $35dB$ and the delay range limited to $60ns$ are utilized to illustrated the main paths.

The PAD profile measured with horn antenna is drawn in Fig. 6 (top). For the virtual UCA measurement, CBF and MFIBF techniques are applied to obtain the PAD profiles, respectively. The beam patterns of CBF and MFIBF can be obtained by substituting $\mathbf{W}(f, \pi/2, \phi)$ into equation (5), where the $\mathbf{W}(f, \pi/2, \phi)$ are defined in (7) and in (11) (with $G_m(f, \theta)$ replaced with $\hat{G}_m(f)$ in (15)), respectively. We can then obtain the PAD profiles of CBF and MFIBF via performing IDFT of $H_F(f, \pi/2, \phi)$ in (6). The PAD profiles with virtual UCA utilizing CBF and MFIBF are plotted in Fig. 6. Note that the PAD profile with conventional FIBF UCA is not shown in Fig.6, since it fails to detect any of the paths. We can see that:

- Both CBF and MFIBF work in the practical 3D scenarios, as expected;
- The same paths (as numbered) are identified for measurements with horn antenna and virtual UCA;
- Better resolutions in angle and delay domains can be achieved for measurement results with virtual UCA;
- The measured results with CBF UCA suffer from high joint sidelobes in angle and delay domains (e.g. sidelobes of path 1 and 4) and the weak paths (e.g. path 2, 9 and 5) are buried by the sidelobes of the strong paths;
- The measured results with MFIBF UCA, narrower main lobes and lower sidelobes can be obtained in angle and

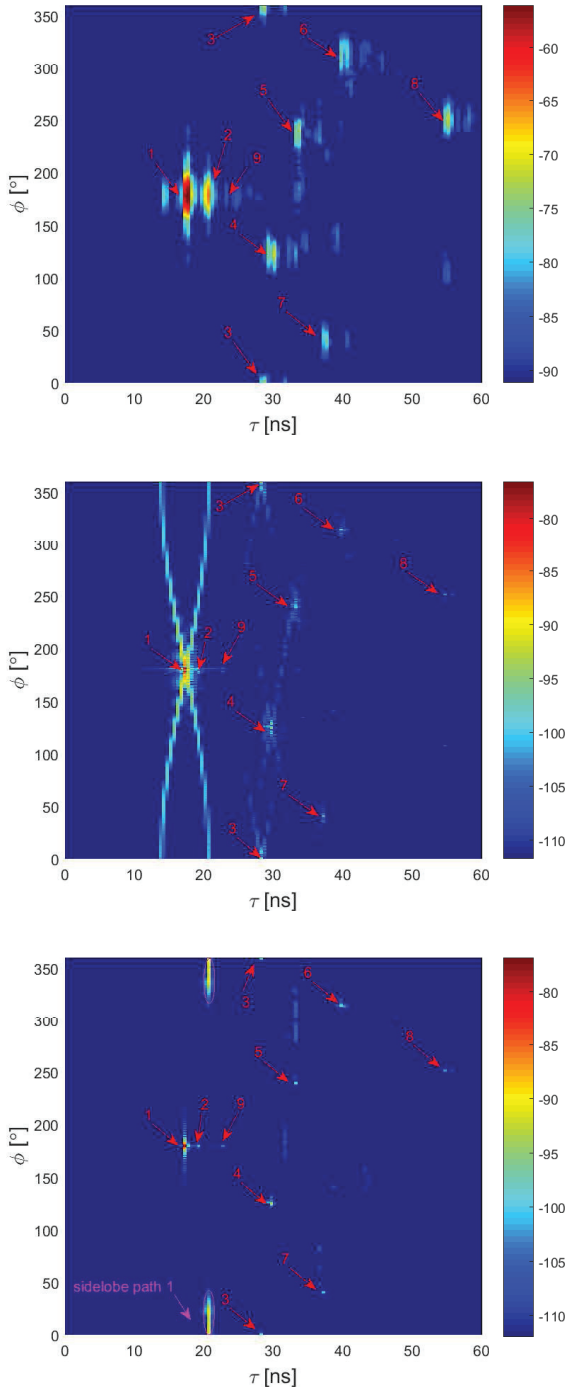

Fig. 6. PAD profile with horn antenna (top), with virtual UCA utilizing CBF (middle) and MFIBF (bottom).

delay domains, though suffer from the sidelobe of path 1 (around 0^o), as explained in Section II.

V. Conclusion

This paper summarize the CBFs and FIBFs for UCA with isotropic antenna elements to estimate wideband multipath parameters in 2D and 3D scenarios. Numerical simulation and measurement results demonstrate that:

- CBF method is robust, since it works for both 2D and 3D multipath scenarios. However, its beam pattern suffers from high joint sidelobes in angle and delay domains, wide mainbeam and frequency dependency;
- Conventional FIBF method can obtain the frequency invariant beam patterns of narrow mainbeam and low sidelobes. Howevet it can only work for 2D scenarios and would fail in practical measurements;
- MFIBF method is robust that it works for both 2D and 3D multipath scenarios and its beam patterns are frequency independent and with narrow mainbeam and low sidelobes. However, it suffers from the sidelobes around $\phi_k = \phi_k + \pi$;
- Horn antenna, works for both 2D and 3D scenarios, via mechanical rotating the horn antenna in azimuth and elevation plane. However, it suffers from wide beamwidth and horn antenna measurements is slow in measurements.

Acknowledgment

This work was supported by the Innovation Fund Denmark via the RANGE Project. The work of Dr. Wei Fan was supported by the Financial assistance from the Danish council for Independent Research under Grant DFF 6111-00525.

References

[1] T. S. Rappaport, S. Sun, R. Mayzus, H. Zhao, Y. Azar, K. Wang, ... and F. Gutierrez, *Millimeter wave mobile communications for 5G cellular: It will work*, IEEE access (1), 335-349, 2013.

[2] S. Salous, V. Degli-Esposti, M. Nekovee and S. Hur, *Review of Millimeter-wave Propagation Characterization and Modelling Towards 5G Systems*, (EuCAP), 2015 9th European Conference on. IEEE, 2015.

[3] T. S. Rappaport, G. R. MacCartney, M. K. Samimi and S. Sun, *Wideband millimeter-wave propagation measurements and channel models for future wireless communication system design*, IEEE Transactions on Communications, 63(9), 3029-3056, 2015.

[4] S. Hur, Y. J. Cho, J. Lee, N. G. Kang, J. Park and H. Benn, *Synchronous channel sounder using horn antenna and indoor measurements on 28 GHz*, Communications and Networking (BlackSeaCom), 2014 IEEE International Black Sea Conference, 83-87, 2014.

[5] C. Gentile, A. J. Braga and A. Kik, *A comprehensive evaluation of joint range and angle estimation in ultra-wideband location systems for indoors*, 2008 IEEE International Conference on Communications, 4219-4225, IEEE, 2008.

[6] M. S. Hossain, G. N. Milford and M. C. Reed, *Efficient robust broadband beamforming using circular antenna arrays*, Communications and Information Technologies (ISCIT), 2012 International Symposium, 746-751, IEEE, 2012.

[7] B. Liao, K. M. Tsui and S. C. Chan, *Frequency invariant uniform concentric circular arrays with directional elements*, IEEE Transactions on Aerospace and Electronic Systems, 49(2), 871-884, 2013.

[8] Balanis, *Antenna theory: analysis and design*, John Wiley & Sons, 2016.

[9] C. Gentile, A. J. Braga and A. Kik, *A comprehensive evaluation of joint range and angle estimation in indoor ultrawideband location systems*, EURASIP Journal on Wireless Communications and Networking, 36, 2008.

[10] F. Zhang, W. Fan and G. F. Pedersen, *Frequency Invariant Uniform Circular Array for Wideband mm-Wave Channel Characterization*, IEEE Antennas and Wireless Propagation Letters, 2016.

[11] I. Carton, W. Fan and G. F. Pedersen, *A frequency invariant beamformer for channel parameter estimation in millimeter wave bands*, 2015 International Symposium on Antennas and Propagation (ISAP), 1-4, IEEE,2015.

[12] W. Fan, I. Carton, J. ∅. Nielsen, K. Olesen and G. F. Pedersen, *Measured wideband characteristics of indoor channels at centimetric and millimetric bands*, EURASIP Journal on Wireless Communications and Networking, 2016 (1), 1-13, 2016.